

This is the author's version of the work. It is posted here by permission of the AAAS for personal use, not for redistribution. The definitive version was published in *Science* on May 8; 368(6491), DOI: [10.1126/science.aaz9634](https://doi.org/10.1126/science.aaz9634).

The full details of the published version of the article are as follows:

TITLE: Aerodynamic Imaging by Mosquitoes Inspires a Surface Detector for Autonomous Flying Vehicles

AUTHORS: Toshiyuki Nakata, Nathan Phillips, Patrício Simões, Ian J Russell, Jorn A Cheney, Simon M Walker, Richard J Bomphrey

JOURNAL TITLE: Science

PUBLISHER: American Association for the Advancement of Science (AAAS)

PUBLICATION DATE: 8 May 2020

DOI: 10.1126/science.aaz9634

1 **Title:**

2 **Aerodynamic imaging by mosquitoes inspires a surface detector for**  
3 **autonomous flying vehicles**

4  
5 **Authors:** Toshiyuki Nakata<sup>1,2†</sup>, Nathan Phillips<sup>1†</sup>, Patrício Simões<sup>3</sup>, Ian J Russell<sup>3</sup>, Jorn A  
6 Cheney<sup>1</sup>, Simon M Walker<sup>4</sup>, Richard J Bomphrey<sup>1\*</sup>

7  
8 **Affiliations:**

9 <sup>1</sup>Structure and Motion Laboratory, Royal Veterinary College, Hawkshead Lane, Hatfield,  
10 UK, AL9 7TA, United Kingdom.

11 <sup>2</sup>Graduate School of Engineering, Chiba University, Chiba, 263-8522, Japan.

12 <sup>3</sup>Pharmacy and Biomolecular Sciences, University of Brighton, Moulsecoomb, Brighton,  
13 BN2 4GJ, United Kingdom.

14 <sup>4</sup>Faculty of Biological Sciences, University of Leeds, Leeds, LS2 9JT, United Kingdom.

15 \*Correspondence to: rbomphrey@rvc.ac.uk

16 †Contributed equally to this work.

17  
18  
19 **Abstract:**

20 Some flying animals use active sense to perceive and avoid obstacles. Nocturnal mosquitoes  
21 exhibit a behavioral response to divert away from surfaces when vision is unavailable,  
22 indicating a short-range, mechanosensory collision avoidance mechanism. We suggest this  
23 behavior is mediated by perceiving modulations of their self-induced airflow patterns as they  
24 enter ground or wall effect. We use computational fluid dynamics simulations of low-altitude  
25 and near-wall flights, based on in vivo high-speed kinematic measurements, to quantify  
26 changes in the self-generated pressure and velocity cues at the sensitive, mechanosensory,  
27 antennae. We validated the principle that encoding aerodynamic information can enable  
28 collision avoidance using a quadcopter with a sensory system inspired by the mosquito. Such  
29 low power sensing systems have major potential for future, safer, rotorcraft control systems.

30  
31  
32 **One Sentence Summary:**

33 Low power sensing of flow fields by mosquitoes can inspire collision avoidance devices.  
34

35 **Main Text:**

36 At night, in caves, or in otherwise visually compromised environments, animal guidance and  
37 control systems must sense and avoid obstacles without relying on optical information.

38 Mechanoreceptors in arthropods are extraordinarily sensitive and diverse (1), and insects  
39 exploit this fully (2), including for the detection of self-induced flows. For example, fields of  
40 unidirectional trichoid sensilla are likely to be a key component of the fused sensory input  
41 used by flying insects to monitor their attitude (3) and changes in forward speed can be  
42 regulated via aerodynamic drag on the antennae (4). In insects, antennal motion is detected by  
43 the Johnston's organ (JO) - an array of chordotonal mechanoreceptors located in the antennal  
44 pedicel. The JO can detect fluid flows, gravitational pull, and acoustic stimulation and it is  
45 one of the most sensitive mechanoreceptive organs in the animal kingdom (5). Mosquitoes,  
46 possess exceedingly sensitive JOs. The radial organization of its ~12,000 mechanoreceptive  
47 units functionally arranged in antiphase pairs (6), allow mosquitoes to respond to antennal  
48 deflections of  $\pm 0.0005^\circ$  induced by  $\pm 11$  nm air particle displacements in the acoustic near  
49 field (*Toxorhynchites brevipalpis*) (7) or to acoustic particle velocities of  $\sim 10^{-7}$  ms<sup>-1</sup> (*Culex*  
50 *quinquefasciatus*) (8).

51 We take inspiration from such neurophysiological evidence and postulate a sensory  
52 mechanism for *C. quinquefasciatus* that can explain recent behavioral experiments that show  
53 mosquitoes avoiding surfaces invisible to their compound eyes (9). The absence of visual  
54 cues indicates that another source of close-range information exists, and we hypothesised that  
55 these alternative cues are manifest within interactions between the fluid and antennae or hair  
56 structures. Specifically, we propose that mosquitoes can detect changes to their self-induced  
57 flow patterns caused by the proximal physical environment. These changes to the downwash  
58 flow patterns initially generated by the flapping wings arise as the jets of air impinge on the  
59 obstacle's surface. This non-contact, sensory modality for flying insects is somewhat akin to

60 the hydrodynamic imaging capability of the lateral line system in fish (*10, 11*), which is also  
61 fundamentally a fluid dynamic, pressure-based system. It would be particularly useful for  
62 mosquitoes, which must be adept at stealthy landings on hosts (*12*) and egg-deposition over  
63 water at night.

64 We demonstrate how nearby surfaces may be detected by mosquitoes by means of the flow  
65 field produced during flapping flight (*13*), which is modulated in response to surfaces at  
66 magnitudes sufficient for detection by their mechanosensors. We implement the governing  
67 principles onto a miniature, flying vehicle operating close to the ground and walls, fitted with  
68 a sensor package that can detect surfaces at distances sufficiently far from collision for  
69 effective obstacle avoidance (Movie S1).

70 Mosquito wingbeat kinematics show high wingbeat frequency, low wingbeat amplitude, and  
71 large, rapid span-wise rotations. These features result in unorthodox aerodynamic flows  
72 around the wings themselves (*13*) and two concentrated jets of fast moving air that merge  
73 approximately two wing lengths beneath the body. By virtue of the shallow stroke amplitude,  
74 the jets are more focused than the wake of other flying animals, which may help to improve  
75 the signal if the interaction of the induced flow with a ground plane is important for collision  
76 avoidance. Building on our previous data set (*13*), we performed further CFD simulations at a  
77 range of distances from either ground or a wall plane to quantify the effect on local flows  
78 around the mosquito (Fig. 1A; S1). Movie S1 shows flow simulations at infinite altitude  
79 (where infinite in this case is flight at an altitude far from a surface) and when the jets  
80 impinge on a ground plane 10 mm below the mosquito.

81 Downwash dominates the flow field at higher altitudes. However, at lower altitudes  
82 (<10mm), the downwash velocity progressively reduces and recirculation can be seen in  
83 some regions, particularly under the body. To see the effect more clearly, we calculated the  
84 wingbeat-averaged pressure deltas for each distance relative to the infinite altitude case (Fig.

85 1C). The zones with the largest pressure deltas are located below the thorax and, surprisingly,  
86 above the head. The antennae, with their sensitive JO at the base (7, 8), are therefore well-  
87 placed to measure subtle changes in the vector strength of particle velocity in the antero-  
88 dorsal region of the head despite being located furthest from the ground. Flow sensitive hairs  
89 along the hind leg femur, and elsewhere, could reasonably detect changes in flow velocity  
90 associated with these pressure changes too, especially at the lower altitudes, although hind  
91 leg hair sensitivity is an order of magnitude lower (Fig. S2). Mosquitoes extend their hind  
92 legs towards a surface when landing, and backwards when flying, and are therefore able to  
93 compliment the JOs to detect pressure differences due to floor and wall effects. The antennae  
94 of flying insects are self-stimulated both by periodic air movements due to wingbeats and by  
95 tonic flow due to translation through the air. Recent mosquito tuning data show two  
96 sensitivity peaks in male JO. One occurs at lower frequencies (centred at ~280 Hz) and it is  
97 tuned to detect the wingbeat frequency of females using an acoustic distortion mechanism  
98 (8). A secondary peak of sensitivity is centred on frequencies similar to those at which males  
99 fly (600-800 Hz) which would enable a male mosquito to hear its own flight and possibly that  
100 of other nearby males (8, 14). Male mosquito JO are therefore adept at perceiving tiny  
101 changes in the direction and magnitude of flow velocity of the type associated with proximity  
102 to surfaces, potentially using one sensitivity band to detect females and another for detecting  
103 changes to their self-generated flow fields when encountering obstacles. In addition to the  
104 ground effect, wall surfaces also modulate the simulated flow field (Fig. 1B). Again, changes  
105 in pressure distribution can be seen above the head and below the thorax, so both floors and  
106 walls could be detected by the same cuticular flow sensors or pressure sensors.

107 At the male wingbeat frequency, the male JO exhibits a local peak in sensitivity and can  
108 detect changes in flow velocities on the order of  $10^{-4} \text{ ms}^{-1}$  (Fig. 1D and SI). We include this  
109 empirically-derived limit on Figures 1D-F, where we present the change in flow velocity at

110 the wingbeat frequency with varying proximity to the ground (Fig. 1E) and the frequency  
111 spectrum of the induced flows (Fig. 1F). Flow velocity oscillates less with altitude, and closer  
112 proximity to the ground does not cause oscillations in the flow experienced by the JO to  
113 deviate from wingbeat frequency. At higher altitudes, differences in the magnitude of  
114 velocity fluctuations at the wingbeat frequency become less pronounced and, for numerical  
115 reasons, CFD will eventually fail to capture the very smallest changes in velocity. There is a  
116 considerable computational burden as the fine mesh extends to ever more distant ground  
117 planes and the velocities deltas tend to zero; nevertheless, a clear trend can be seen whereby  
118 the JO can easily detect changes at low altitude but with a diminishing response as the  
119 altitude increases until the threshold for detection is not met (Fig. 1E).

120 The intercept of the CFD-derived velocity changes and the measured sensitivity of the JO  
121 predicts a maximum surface detection distance in *Culex* mosquitoes of 36.4 mm or 20.2 wing  
122 lengths. This is a conservative estimate as it only considers the content of the flow signature  
123 at wingbeat frequency. Intriguingly, this distance predicted for *Culex* males is broadly  
124 consistent with egg-laying dipping behavior in female *Anopheles*, where they dip to altitudes  
125 of 20-70 mm above the water surface (9). Detection of a ground plane at such distances is far  
126 in excess of that which might be expected by the ground effect typically referred to in the

127 aerodynamic literature, where notable improvements in lift and drag force characteristics of  
128 wings become negligible beyond an altitude of a single wing length or rotor radius. In our  
129 mosquitoes, the negative pressure delta region observed above the head and under the thorax  
130 when close to the floor occurs as a result of increasing unsteadiness of the flow in this region,  
131 leading to higher peak velocities and lower pressures (Fig. 1C). Conversely, away from  
132 surfaces, the flow around the body is relatively steady as the speeds of the wing bases are  
133 low.

134 Mosquitoes are not known to have pressure receptors that could monitor the reflected sound  
135 from nearby surfaces in the same manner as echolocating animals. While we do not rule out  
136 the possibility that the JO could detect the reflected particle velocity component of self-  
137 induced sounds, it would be less useful than the pressure component since the particle velocities  
138 decrease with the inverse cube of distance rather than the inverse square. Moreover, the  
139 frequency of the flight tone means that the wavelength of the acoustic signature is relatively  
140 large, on the order of 0.5—1.0m, which limits precision in locating a surface. By contrast,  
141 typical echolocation in gleaning bats uses frequencies in the tens of kilohertz, giving a  
142 superior resolution by two orders of magnitude. Given the relatively large changes in particle  
143 velocity induced by each wingbeat that can comfortably be detected by the JO at altitudes of  
144 many body lengths, we offer that this is a more robust solution to surface detection than  
145 echolocation.

146 To show how mechanosensory flow-field monitoring can be used in collision avoidance in  
147 autonomous systems, we fitted a small quadcopter platform with a bio-inspired sensor that  
148 can detect floors and walls using physical principles similar to those described  
149 above: specifically, modulation of a deforming flow field. It is lightweight, power-efficient  
150 and stealthy, with no additional emission of light or electromagnetic radiation necessary. It is

151 also applicable to rotorcraft or flappercraft of any scale and can work in conditions that are  
152 unsuited to alternative range-finding tools. We instrumented an existing 27 g platform  
153 (Crazyflie 2.0, Bitcraze, Sweden), with custom circuits and algorithms to identify obstacle  
154 proximity based on pressure sensor readings. The stand-alone sensor module performs  
155 reliable obstacle detection up to three rotor diameters away during autonomous flights.  
156 The device, like the mosquito, will be most sensitive if sensors are mounted at locations  
157 experiencing the greatest changes in the flow field when approaching surfaces. Nearby  
158 surfaces distort the flow field all around the body – making surface detection simple, direct

159 and robust – but, to determine optimal sensor design, number and placement, it is necessary  
160 to find the most affected regions. We used stereo particle image velocimetry to measure fluid  
161 velocities around the quadcopter at various altitudes and proximities to a wall (Fig. 2; S3).  
162 These flow measurements were used to inform the position of probe tubes relative to the  
163 annular jets and regions of recirculation under the control boards. The probes were connected  
164 to differential pressure sensors, which are a more accessible solution than particle-velocity  
165 probes (Fig. 3; S4-7). Since the dynamic pressure is proportional to the square of flow  
166 velocity the same physical phenomenon underpins the sensing capability. Ground effect  
167 could be detected using a pair of probes extending above and below the craft, while the  
168 direction of nearby walls could be detected by using paired probes extending fore-aft,  
169 laterally, or diagonally. Further detail on the design criteria and the pressure delta thresholds  
170 for each proximity condition are detailed in Supplementary Material.  
171 This simple model could detect both ground and wall effects. Pressure differential increases  
172 with surface proximity (Fig. 3F-G) and of sufficient signal to provide alarm thresholds (Table  
173 S1,S3) for each proximity condition. The complete module weighed just 9.2g (see Table S2  
174 for detailed mass breakdown).  
175 The device successfully emulated the mosquito model behavior by identifying nearby

176 obstacles during flight. Initially the quadcopter was flown tethered (Fig. 4A-B), then piloted  
177 (Fig. 4C) and, finally, autonomously using positional feedback from a motion capture system.  
178 Ground (Fig. 4D; S9-10) and wall planes (Fig. 4E-G) could be discriminated using  
179 appropriately placed sensor combinations monitoring induced flow field changes. Previous  
180 quadcopter studies have detected proximal surfaces by combining measured rotor speeds  
181 required for stable hovering with an aerodynamic model of the rotor and the motor speed  
182 required to support weight (15). Others have detected external flows such as fans emulating  
183 the downwash of another vehicle (16) or successfully incorporated flight dynamics models of

184 the specific quadcopter platform and used them to infer obstacle proximity by the forces and  
185 torques acting on the vehicle (17). Our method requires no a priori aerodynamic or rigid body  
186 models to function, but rather requires only basic thresholds. It is therefore a more direct  
187 measure of surface proximity and needs little or no processing to function.

188

189

190 **References**

191

- 192 1. F. G. Barth, *A Spider's World: Senses and Behavior*. (Springer, Berlin, 2002).
- 193 2. M. C. Göpfert, R. M. Hennig, Hearing in Insects. *Annu. Rev. Entomol.* **61**, 257-276  
194 (2016).
- 195 3. G. K. Taylor, H. G. Krapp, in *Advances in Insect Physiology: Insect Mechanics and*  
196 *Control*. (2008), vol. 34, pp. 231-316.
- 197 4. T. Roy Khurana, S. P. Sane, Airflow and optic flow mediate antennal positioning in  
198 flying honeybees. *eLife* **5**, e14449 (2016).5. L. H. Field, T. Matheson, in *Adv. Insect*  
199 *Physiol.*, P. D. Evans, Ed. (Academic Press, 1998), **27**, pp. 1-228.
- 200 6. D. N. Lapshin, D. D. Vorontsov, Directional and frequency characteristics of auditory  
201 neurons in *Culex* male mosquitoes. *J. Exp. Biol.* **222**, jeb208785 (2019).
- 202 7. M. C. Göpfert, H. Briegel, D. Robert, Mosquito hearing: sound-induced antennal  
203 vibrations in male and female *Aedes aegyptii*. *J. Exp. Biol.* **202**, 2727-2738 (1999).
- 204 8. P. M. V. Simões, R. A. Ingham, G. Gibson, I. J. Russell, A role for acoustic distortion  
205 in novel rapid frequency modulation behavior in free-flying male mosquitoes. *J. Exp.*  
206 *Biol.* **219**, 2039-2047 (2016).
- 207 9. F. Hawkes, G. Gibson, Seeing is believing: the nocturnal malarial mosquito

- 208            *Anopheles coluzzii* responds to visual host-cues when odour indicates a host is nearby.  
209            *Parasites & Vectors* **9**, 320 (2016).
- 210    10.    S. Dijkgraaf, The functioning and significance of the lateral-line organs. *Biol. Rev.* **38**,  
211            51-105 (1963).
- 212    11.    M. Yoshizawa, W. R. Jeffery, S. M. van Netten, M. J. McHenry, The sensitivity of  
213            lateral line receptors and their role in the behavior of Mexican blind cavefish  
214            (*Astyanax mexicanus*). *J. Exp. Biol.* **217**, 886-895 (2014).

- 215 12. F. T. Muijres *et al.*, Escaping blood-fed malaria mosquitoes minimize tactile detection  
216 without compromising on take-off speed. *J. Exp. Biol.* **220**, 3751-3762 (2017).
- 217 13. R. J. Bomphrey, T. Nakata, N. Phillips, S. M. Walker, Smart wing rotation and  
218 trailing-edge vortices enable high frequency mosquito flight. *Nature* **544**, 92-95  
219 (2017).
- 220 14. D. N. Lapshin, Mosquito bioacoustics: auditory processing in *Culex pipiens pipiens* L.  
221 males (Diptera, Culicidae) during flight simulation. *Entomol. Rev.* **92**, 605-621  
222 (2012).
- 223 15. C. Powers, D. Mellinger, A. Kushleyev, B. Kothmann, V. Kumar, in *Experimental*  
224 *Robotics: The 13th International Symposium on Experimental Robotics*, J. P. Desai,  
225 G. Dudek, O. Khatib, V. Kumar, Eds. (Springer International Publishing, Heidelberg,  
226 2013), 289-302.
- 227 16. D. W. Yeo, N. Sydney, D. A. Paley, D. Sofge, Downwash detection and avoidance  
228 with small quadrotor helicopters. **40**, 692-701 *J. Guidance, Control and Dynamics*.  
229 (2016).
- 230 17. C. D. McKinnon, A. P. Schoellig, Estimating and reacting to forces and torques  
231 resulting from common aerodynamic disturbances acting on quadrotors. *Robot. Auton.*  
232 *Syst.* 103314 (2019).

- 233 18. H. Liu, Integrated modeling of insect flight: from morphology, kinematics to  
234 aerodynamics. *J. Comput. Phys.* **228**, 439-459 (2009).
- 235 19. S. M. Walker, A. L. R. Thomas, G. K. Taylor, Operation of the alula as an indicator  
236 of gear change in hoverflies. *J. R. Soc. Interface*, **9**, 1194-1207 (2011).
- 237
- 238

239 Supplementary Materials only:

240

241 20. T. Nakata, H. Liu, Aerodynamic performance of a hovering hawkmoth with flexible  
242 wings: a computational approach. *Proc. R. Soc. B* **279**, 722-731 (2012).

243 21. M. C. Göpfert, D. Robert, Active auditory mechanics in mosquitoes. *Proc. Biol. Sci.*  
244 **268**, 333-339 (2001).

245 22. B. Warren, A. N. Lukashkin, I. J. Russell, The dynein-tubulin motor powers active  
246 oscillations and amplification in the hearing organ of the mosquito. *Proc. R. Soc. B*  
247 **277**, 1761-1769 (2010).

248

249

250

251 **Acknowledgements:**

252 The authors are grateful for discussions with the RVC flight group, P. Kimber and C. Jones  
253 of Dstl and N. Short. We thank Professor H. Liu of Chiba University for permission to use  
254 the CFD simulator. **Funding:** This work was funded, in part, by the Autonomous Systems  
255 Underpinning Research (ASUR) programme under the auspices of the Defence Science and  
256 Technology Laboratory (Dstl), UK Ministry of Defence and, in part, by the Biotechnology  
257 and Biological Sciences Research Council (BB/J001244/1), both to RJB. SMW was  
258 supported by a Royal Society University Research Fellowship. Work at the University of  
259 Brighton was funded by the Medical Research Council (MR/ N004299/1). PS was partly  
260 supported by the Rising Stars award from the University of Brighton. **Author contributions:**  
261 RJB conceived the experiments with TN, NP, SMW and IJR. SMW, IJR and PS advised on  
262 experimental protocol. NP designed and built the quadcopter sensor module. NP and JC built  
263 quadcopter module communication links. IJR and PS gathered and processed data for the JO  
264 and femoral hairs. RJB, TN, NP and SMW wrote the manuscript. All authors contributed to  
265 editing the manuscript.

266 **Competing interests:** Some of this work was used to support, in part, patent filing WO  
267 2019/002892 A1. **Data and materials availability:** All data is available in the main text or

268 the supplementary materials. Mosquito kinematics are available via (13). The CFD solver  
269 (18) and kinematics acquisition code (19) are described in further detail elsewhere.  
270

271

272 **Fig. 1.** Velocity and pressure distributions around mosquitoes flying near surfaces. A) Front  
273 view of a mosquito hovering at five altitudes measured from the mosquito body with  
274 downwash shown in blue and the upwash in red. Flow visualisation plane at maximum  
275 wingspan. A discrete jet from each wing merges in the infinite and high altitude cases. B,C)  
276 Side view of a hovering mosquito (grey), and distribution of absolute wingbeat-averaged  
277 mean difference in pressure relative to the infinite case  $\overline{|\Delta P|}$  (Pa), measuring in the sagittal  
278 plane. The pressure distribution in free airspace is compared to flight B) near a wall (where  
279 the wall is the left edge of the panel), and C) at varying altitudes; white cross shows  
280 monitoring location corresponding to the tip of the antenna. D) The particle velocity detection  
281 threshold of the male JO shows a secondary notch of enhanced sensitivity (white arrow)  
282 within the male wingbeat frequency range (see supplementary material for electrophysiology  
283 methods and also (8)). Grey shading indicates the range of male wingbeat frequencies  
284 observed during free flight. The JO's secondary notch has a particle velocity sensitivity  
285 shown by the solid line. The primary notch at approximately 200 Hz is used for mating  
286 communication and is tuned to tones generated by the male-female wingbeat frequencies'  
287 distortion product. E) The amplitude of change in velocity magnitude at wingbeat frequency  
288 measured at the antennae increases with proximity to the ground. A straight line of best fit is

289 plotted (blue, with dashed 95% confidence intervals) to show the intersection with the JO  
290 flow velocity sensitivity at the male wingbeat frequency alone (solid horizontal line). F) The  
291 amplitude of changes in velocity magnitude at the antennae in the frequency domain,  
292 calculated as the Fast Fourier Transform at infinite altitude subtracted from the FFT at a  
293 given altitude over 50 wingbeat cycles. Differences are always greatest at wingbeat  
294 frequency, irrespective of altitude. Asterisk shows JO particle velocity sensitivity at wingbeat  
295 frequency.

296

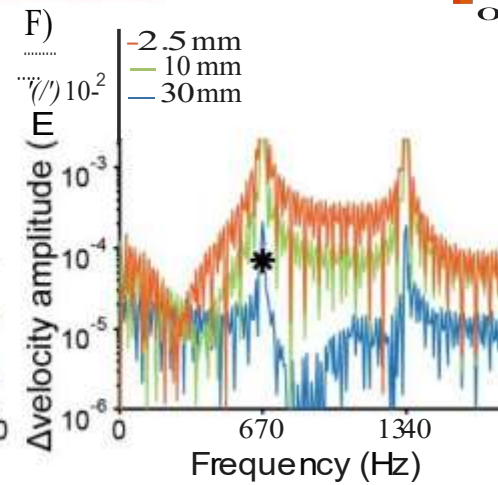
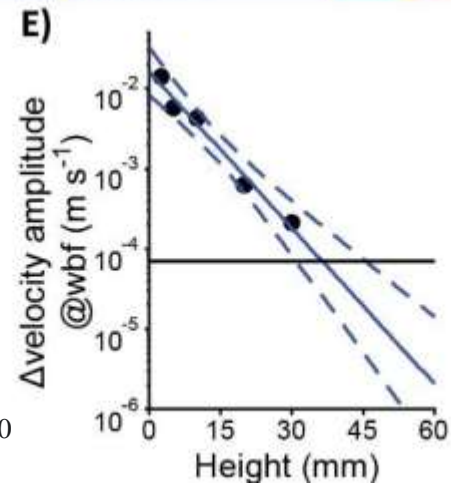
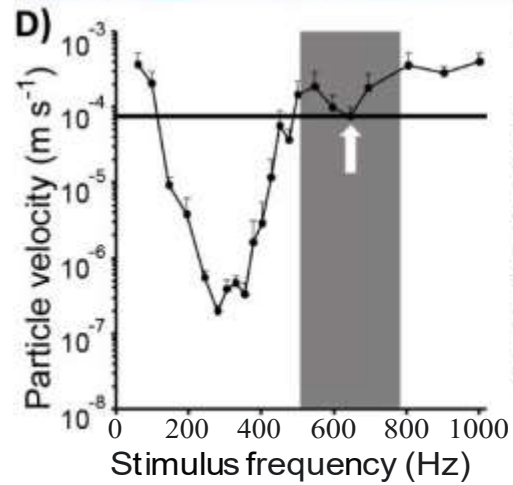
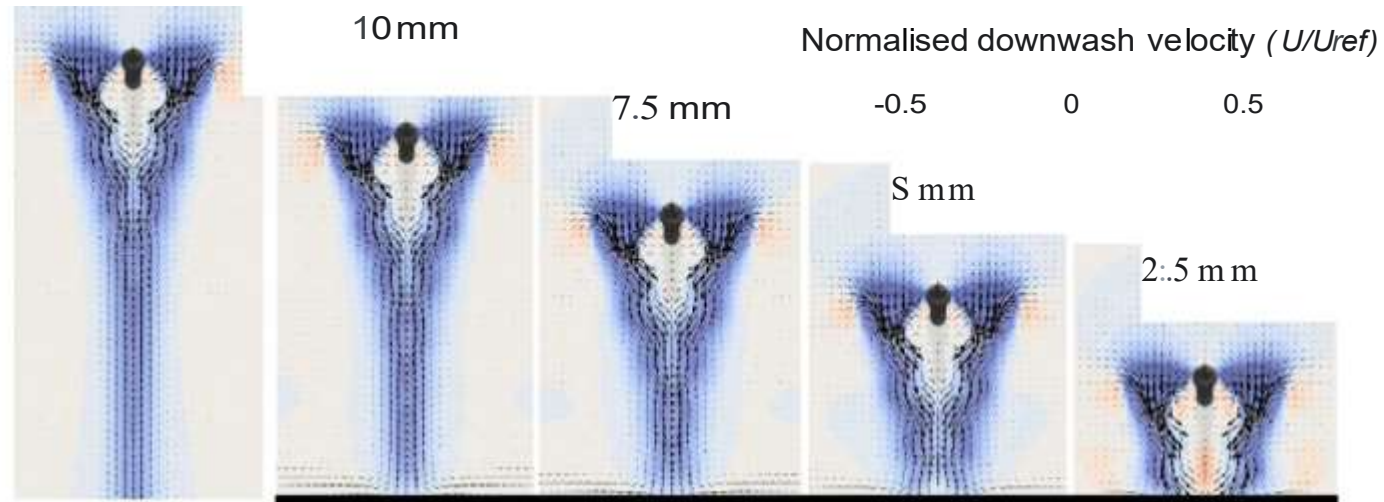
297

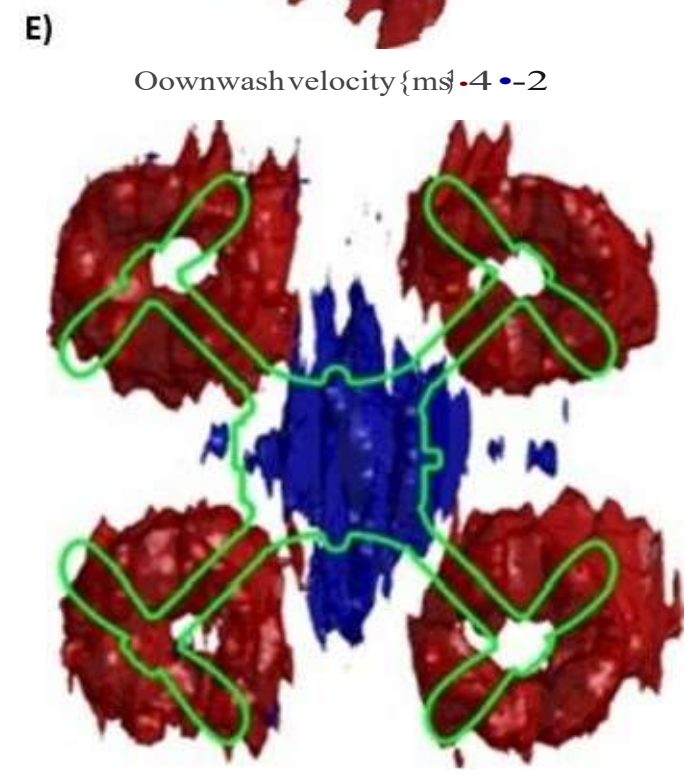
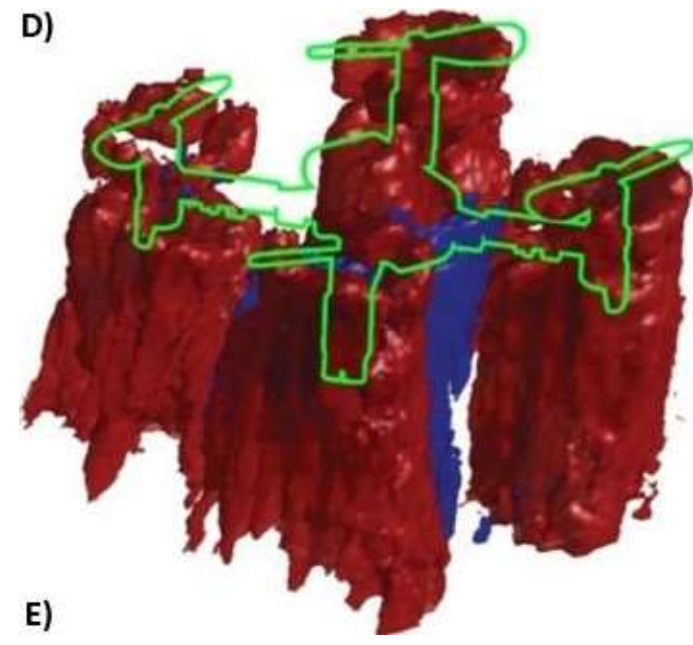
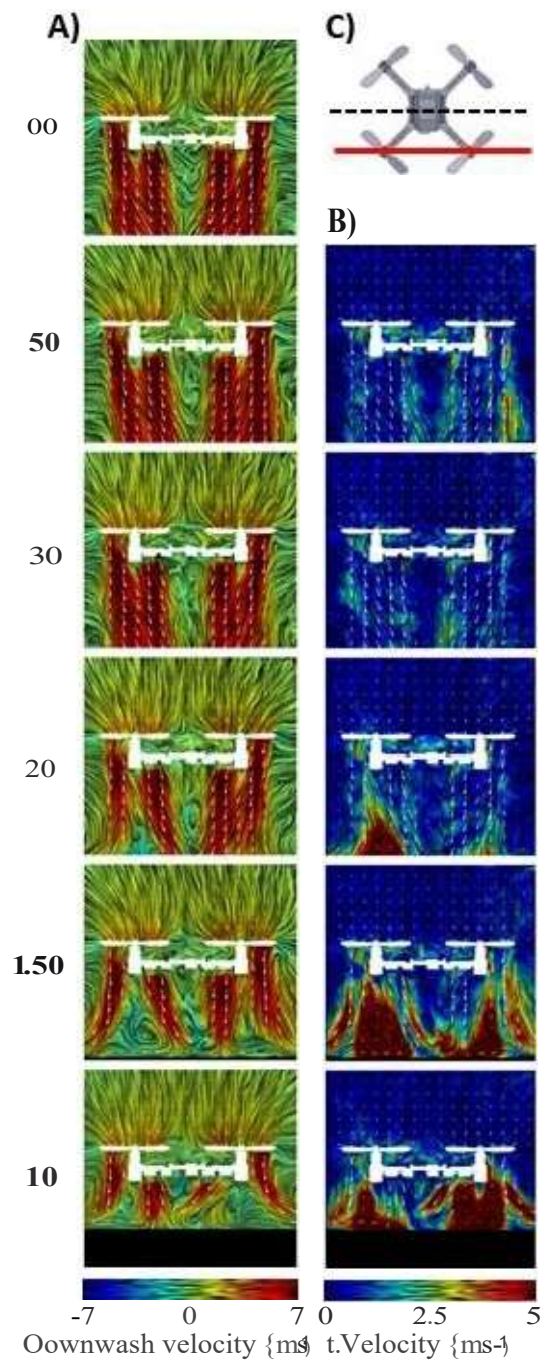
298 **Fig. 2.** Quadcopter flow field characterisation. A) Slices showing induced downwash for a  
299 quadcopter hovering at a range of altitudes in multiples of rotor diameter ( $D = 46\text{mm}$ ). Line  
300 integral convolution shows instantaneous streamlines and color flood shows vertical velocity.  
301 B) Difference in velocity magnitude at altitude range of altitudes. C) Schematic of the craft  
302 showing the PIV measurement plane (red) with respect to a centreline (dashed). D) Oblique  
303 and E) Top view of the three-dimensional flow field at altitude of  $2D$ . Four annular jets  
304 emanate from the rotors and recirculate under the fuselage (iso-surface of downwash and  
305 upwash:  $4\text{ ms}^{-1}$  in red;  $-2\text{ ms}^{-1}$  in blue). Outline of the quadcopter in green, for reference.  
306

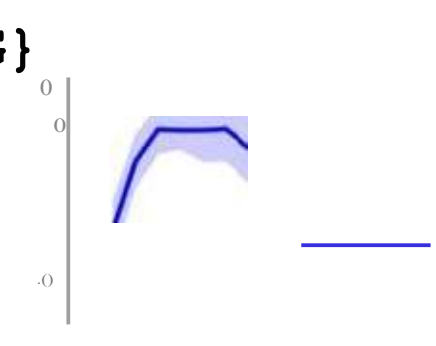
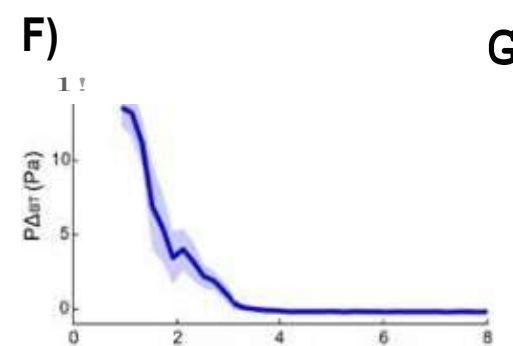
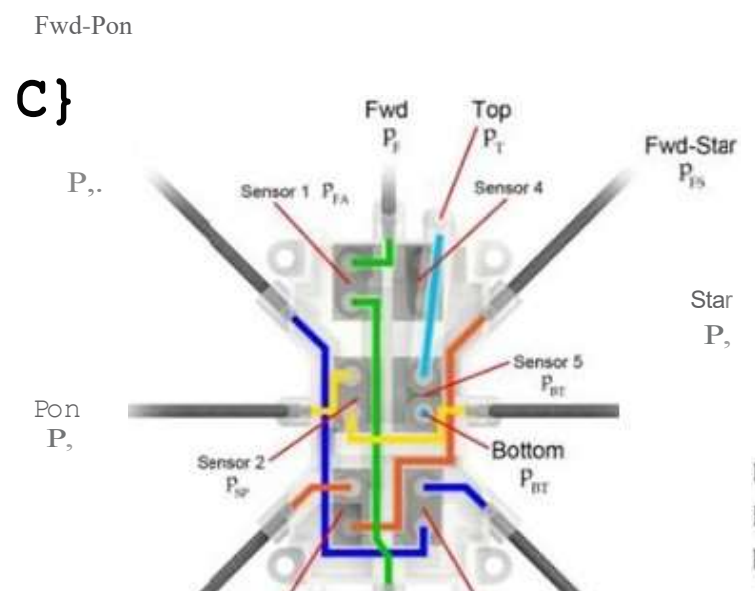
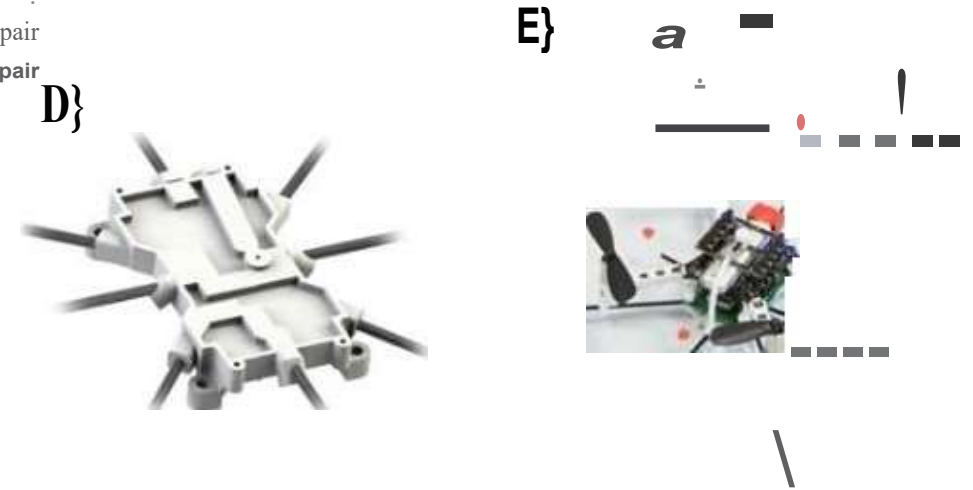
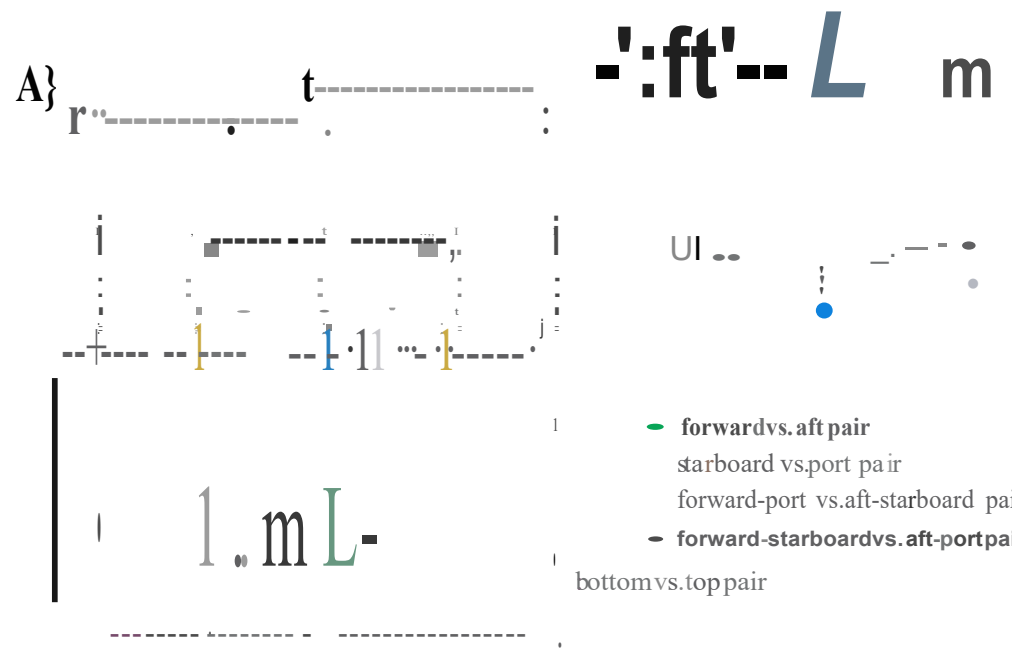
307 **Fig. 3.** Bio-inspired sensor module. A) arrangement and placement of five paired pressure  
308 probes placed to maximise pressure deltas when close to surfaces; B) pressure sensor  
309 module components comprising the pressure sensor array, adapter PCB and  
310 microcontroller; C) schematic showing internal routing tracks connecting paired probes  
311 [Fore-Aft in green, Port-Starboard in yellow, ForwardPort-AftStarboard in dark blue,  
312 ForwardStarboard-AftPort in orange, Top-Bottom in light blue] to pressure sensors via a  
313 tube network shown in D); E) free flying prototype with mosquito-inspired surface detection  
314 device; F,G) Differential pressure delta with proximity to ground (F) and wall (G); shaded  
315 regions indicate one standard deviation. Altitude is measured from the plane of the rotor  
316 hubs. Wall proximity is measured from the nearest rotor hub.  
317

318 **Fig. 4.** Demonstration of aerodynamic imaging in a quadcopter. A) tethered wall proximity  
319 test with wall on forward side of quadcopter. Yellow triangles point at forward and aft red  
320 indicator lights; B) tethered ground proximity test. Yellow arrows show all four red alarm  
321 lights illuminating when ground is detected; C) piloted free flight test of ground detection;  
322 D) long exposure photographs of autonomous test of ground detection. Oblique side view  
323 showing perpetual flight lights in blue, detection indicator lights in red. The ground was  
324 detected twice; E-G) top view of three wall detection trials. A single surface detection  
325 indicator light illuminates on one side nearest the wall before the quadcopter moves away  
326 from the obstruction. A strobe flash prior to the end of the exposure captures the  
327 quadcopter towards the end of its flight.

A) Infinite



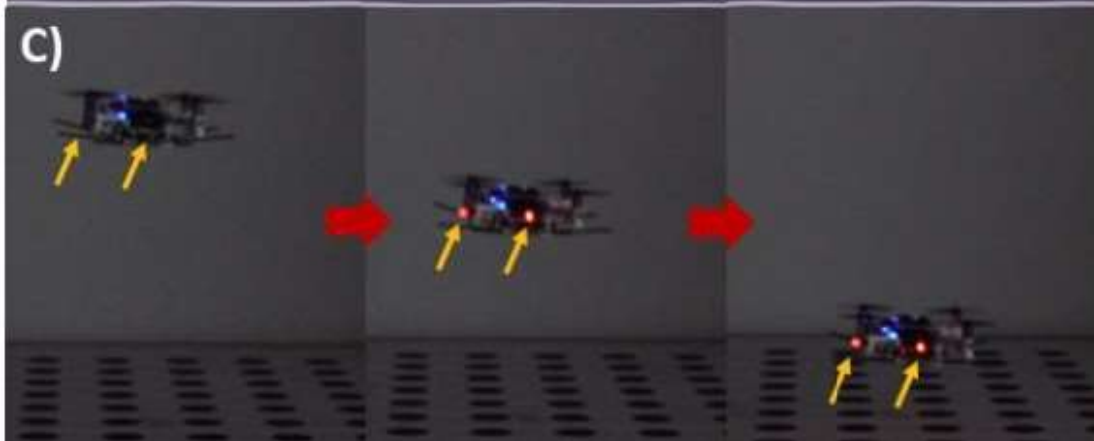
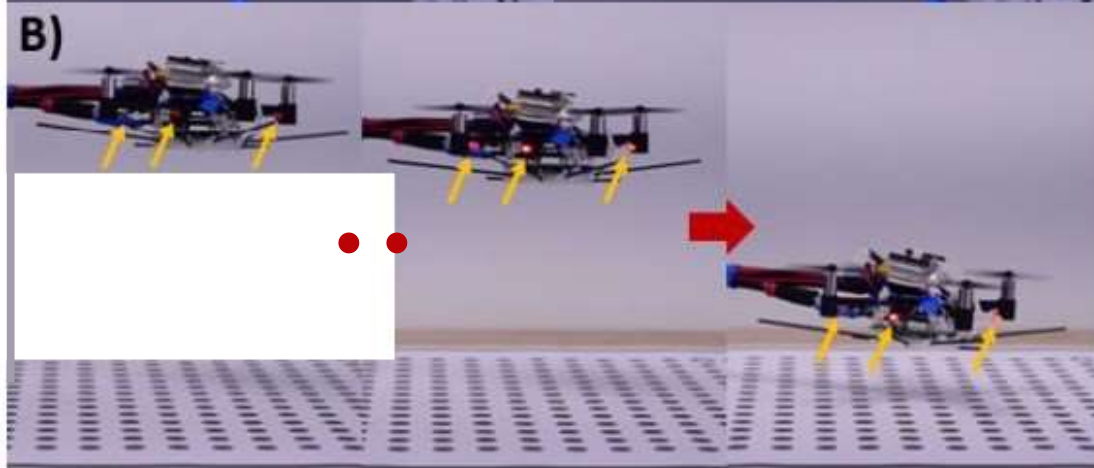
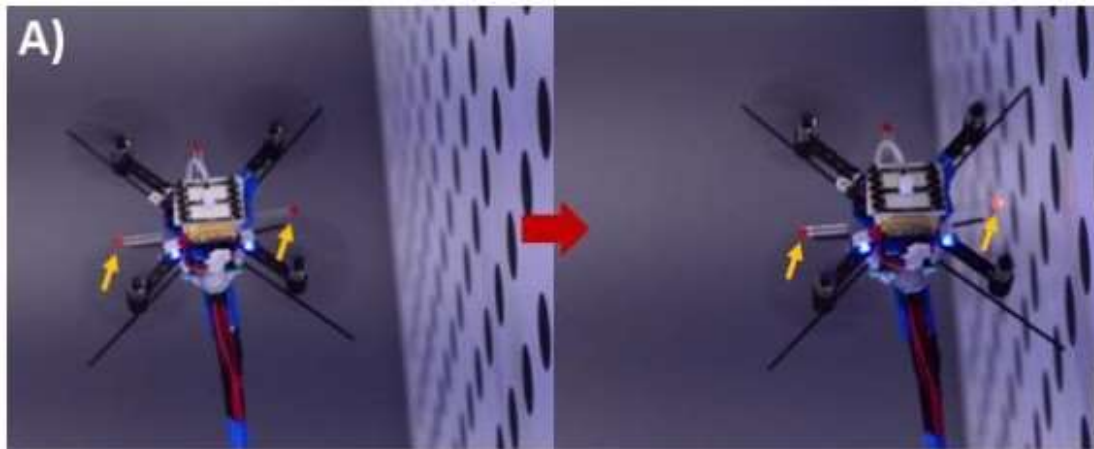




Aft-Port  
||..

Aft-Star  
E,.





1  
2  
3  
4 **Supplementary Materials for**  
5 **Aerodynamic imaging by mosquitoes inspires a surface detector for**  
6 **autonomous flying vehicles**

7  
8 Toshiyuki Nakata<sup>1,2†</sup>, Nathan Phillips<sup>1†</sup>, Patrício Simões<sup>3</sup>, Ian Russell<sup>3</sup>, Jorn A Cheney<sup>1</sup>, Simon M Walker<sup>4</sup>,  
9 Richard J Bomphrey<sup>1\*</sup>

10  
11 Correspondence to: [rbomphrey@rvc.ac.uk](mailto:rbomphrey@rvc.ac.uk)

12  
13  
14  
15 **This PDF file includes:**

16 Materials and Methods  
17 Figs. S1 to S10  
18 Tables S1 to S3  
19 Captions for Movie S1  
20

21  
22  
23 **Other Supplementary Materials for this manuscript include the following:**

24 Movie S1  
25

## 26 **Materials and Methods**

27

### 28 Computational Fluid Dynamics

29

30 For our CFD model, we used a dynamic flight simulator based on the incompressible,  
31 unsteady, three-dimensional Navier-Stokes equations (13, 18, 20). Implementation of the  
32 CFD solver is outlined and validated for insect-scale fluid dynamics in (18). By using a  
33 validated CFD solver, our results should be solver agnostic and similarly validated solvers  
34 should produce comparable results. The simulator utilizes a multi-block, overset-grid method  
35 in which the computational domain is decomposed into the local grid, clustered in the vicinity  
36 of the wings and body, and a global Cartesian grid. The wing and body grids were generated  
37 from a surface mesh acquired using a voxel carving technique (19). The minimum grid  
38 spacing from the surface is based on  $0.1/\sqrt{\text{Re}}$ , where Re is the Reynolds number. The  
39 distance between the surface and outer boundary was set to be  $2.0 c_m$  (mean chord lengths)  
40 for the wings and  $1.0 c_m$  for the body grids. The outer boundary conditions for local grids are  
41 given by a Cartesian background grid ( $28R \times 14R \times 28R$ ). We assumed a symmetric motion  
42 of the left and right wings, and applied a symmetric boundary condition at the sagittal plane  
43 of the body and background grids. The wing grid regenerated every time-step after the wing  
44 surface twisted and rotated around the hinge. Flapping angles were interpolated by a fifth  
45 order Fourier series.

46 Sequences other than those at infinite altitude required a fine mesh ( $0.02 c_m$ ) extending to the  
47 ground plane. This gave sufficient resolution in computing the complex flow interactions in  
48 these regions with the consequence of substantially increased simulation time. Flow fields  
49 were computed for several flight altitudes of: infinite altitude, 5.4 (30 mm), 3.6 (20 mm), 1.8

50 (10 mm), 1.35 (7.5 mm), 0.9 (5 mm) and 0.45 (2.5 mm) wing lengths from the ground.  
51 Standardised wing kinematics were used for all simulations, selected by identifying the mean  
52 kinematics of the individual with kinematics closest to the mean of all individuals measured.  
53 The kinematics and detailed description of their acquisition are available in (13).

54

#### 55 Convergence of the flow field calculations to a steady periodic result

56

57 For the simulation to converge on a steady solution, it was necessary to calculate a sufficient  
58 number of wingbeats such that the flow could convect to the ground plane, interact with the  
59 surface, and subsequently propagate back up to the mosquito. Unsurprisingly, this duration  
60 varied with altitude and, again, processing time increased greatly with distance on account of  
61 the larger volume of fine resolution mesh. Our convergence metric was the difference in  
62 mean flow velocity (in comparison with the infinite altitude case) at a location in the  
63 simulated flow field corresponding to the tip of one antenna (Fig. S1).

64

#### 65 Sensitivity data

66

#### 67 *Johnston's Organs (JO)*

68 Male *Culex quinquefasciatus* mosquitoes (N=6) were immobilized by cold narcosis and fixed  
69 with beeswax to a 5mm side brass block. The pedicel, head and legs were immobilized using  
70 superglue. Acoustic stimuli were delivered to the preparation from a modified DT48  
71 headphone speaker, coupled to a 7mm (internal diameter) plastic tube. The point of the tube  
72 was positioned at the level of the mosquito head and at 10 mm from the tested antennae (8).

73 Compound extracellular receptor potentials were measured from the JO with tungsten  
74 electrodes (5–7M $\Omega$ , 1  $\mu$ m tip, part no. WE30032.OH3, MicroProbes, Gaithersburg, MD,  
75 USA) that were advanced with a Märzhäuser PM10 (GmbH) manipulator so that the tip of  
76 the electrode just penetrated the wall of the pedicel. In this location, voltage responses from  
77 the JO are dominated by compound, phasic receptor potentials from the scolopidia that are  
78 twice the frequency of the acoustic stimulus. All measurements were made on a vibration-  
79 damped table (model: M-VW-3036-OPT-99-9-28-92, Newport Corporation) inside an IAC  
80 sound-attenuated booth.

81 Signals from the electrodes were amplified (10,000-fold) and low-pass filtered (5 kHz) using  
82 a custom-built differential pre-amplifier. Pure tones of 82 ms duration with 8 ms rise/fall time  
83 were delivered via a 5 kHz low-pass filter and calibrated against a known 94 dB sound  
84 pressure level (21) using a Bruel & Kjaer 4230 microphone. Voltage signals for the sound  
85 system were generated and voltage signals from the electrodes were digitized at 250 kHz via  
86 a Data Translation 3010 D/A A/D card using programs written in Matlab. Raw data and  
87 online computation of the magnitude and phase of the phasic voltage signals were stored in  
88 ASCII files for display and further analysis. All recordings were made within 30 min of  
89 preparation to ensure optimal physiological state and hearing sensitivity. Temperature control  
90 for the experiments was provided by placing the mosquito preparation in a chamber  
91 machined in a Peltier-controlled heat sink (22). Current was fed to the Peltier element by a  
92 power supply with a negative feedback control from a thermistor (80TK, Fluke) which was  
93 thermally coupled to the chamber.

94 We recorded and measured the magnitude of the fundamental frequency component of the  
95 extracellular electrical responses from the JO as a function of stimulus level (particle  
96 velocity) to pure sinusoidal tones between 61 and 1001 Hz. The threshold sensitivity for each

97 stimuli frequency was obtained by determining the particle velocity threshold at which the  
98 electrical signal elicited a response 5 dB above the noise floor of the recording.

99

#### 100 *Femoral trichoid sensilla*

101 We used a similar method to measure the velocity response characteristics of femoral hair  
102 flow sensors at a range of frequencies for five male *C. quinquefasciatus* mosquitoes. The  
103 sensitivity peaks at lower frequencies than those of the JO and they are less sensitive overall  
104 (Fig. S2). They are an order of magnitude less sensitive once the frequency exceeds 120Hz,  
105 and relatively insensitive above 300Hz, indicating they are more receptive to a low  
106 frequency, or even DC component of the recirculating flow.

107

#### 108 Quadrotor flow fields

109

110 We measured detailed flow fields produced by the Crazyflie 2.0 quadcopter at a range of  
111 floor and wall proximities using stereo particle image velocimetry (stereo-PIV). The  
112 experimental setup is illustrated in Figure S3, where a pair of stereo 1024 x 1024px high-  
113 speed cameras (Photron SA3, Photron Europe, Ltd) captured seeding particles in a ~1mm  
114 thick light sheet. Illumination was provided by a 527nm 1kHz Nd:YLF laser (Litron LDY-

115 300PIV, Litron Lasers, Ltd. UK) with the beam passing through light sheet optics to focus the  
116 beam and diverge in a single axis. A spherical mirror was used to reflect the laser light sheet  
117 back within the same plane to illuminate shadowed areas cast by the quadcopter, thus giving  
118 comprehensive illumination around the craft.

119 Seeding droplets of olive oil ( $\sim 1\mu\text{m}$ ) were emitted by an aerosol generator and allowed to  
120 become quiescent in a large tented enclosure that contained the particles. The two cameras

121 were fitted with 105mm lenses (AF Nikkor, f2.8) with one camera aligned normal to the light  
122 sheet, and the second camera viewing at approximately 45° angle from normal, requiring a  
123 Scheimpflug lens mount to maintain focus across the measurement plane.

124 A Perspex sheet (1 × 1 m) stiffened with an aluminium angle frame served as a floor or wall  
125 surface. For wall tests, we simply rotated the quadcopter 90° from its typical horizontal  
126 attitude. The height of the surface could be adjusted to set the floor / wall distance from the  
127 quadcopter. The reflective surface of this boundary, and its transparency, minimized  
128 scattered glare. This procedure allowed flow field measurements to be recorded successfully  
129 very close to the surface: within approximately 1 mm.

130 The quadcopter was mounted at its aft end to a sting connected to a traverse, which enabled  
131 translation in 2 mm increments relative to the measurement plane. Thus, the entire volume (of  
132 85 measurement planes) around the quadcopter could be measured, resulting in a dense 3D  
133 grid of three-component flow velocity vectors. A microcontroller traversed the quadcopter at  
134 set distance and time intervals, and also triggered the stereo-PIV measurement via a high-  
135 speed controller. Flow field measurements for a given floor or wall distance configuration  
136 were completely automated and repeatable.

137 During flow characterisation measurements, the quadcopter motors were powered by an

138 external power supply and driven at a frequency of 230 Hz, which corresponded to a thrust  
139 equivalent to the quadcopter weight far from the ground. At each flow field measurement  
140 location across the craft, 12 stereo-PIV measurements were captured at a frequency of 250  
141 Hz. This rate avoided phase-locking of the rotor blades and gave unbiased time-averaged  
142 velocity values. The measurement area was calibrated with a dual-plane  $105 \times 105$  mm  
143 calibration plate. This enabled the raw image pairs to be processed into three-component  
144 vector maps using DaVis 8.0.8 (LaVision UK Ltd, Oxfordshire). For processing, a stereo  
145 cross-correlation algorithm was used with an initial interrogation window size of  $32 \times 32$  px

146 progressing to a final window size of  $16 \times 16$  px with a 50% overlap and deformable  
147 windows. Between passes, a median filter was used to identify and remove spurious vectors,  
148 where vector components of twice the RMS value of their neighbouring components were  
149 considered outliers. After processing, any regions with empty spaces were filled via  
150 interpolation. Finally, the 12 vector maps for each of the 85 planes across the craft were  
151 ensemble-averaged and arranged into a 3D volume.

152

### 153 Sensor module design

154

155 The key element of the pressure sensor module is the pressure sensor array for monitoring the  
156 near pressure field. We designed a custom PCB fitted with six digital differential pressure  
157 sensors (model SDP31 Sensirion Inc.) with a measurement range of  $\pm 500$  Pa, 16 bit  
158 resolution, and a mass of 0.2 g each (Fig. S2).

159 A pressure probe routing component was designed and fabricated with internal tracks  
160 maintaining a fluid connection to their corresponding differential pressure sensors (Fig. S5).

161 This component allowed the probes to be positioned in regions of high velocity deltas for  
162 improved surface detection signal-to-noise. Routes and connections are shown in Figure S5b,

163

wh the probe locations are labelled along with their symbol 'p<sub>i</sub>' denoting the pressure at  
ere  
164 the i<sup>th</sup> probe location. For a given sensor measuring the differential pressure of probe 'i'  
165 relative to probe 'j', the resulting pressure reading p<sub>ij</sub> for that sensor is computed as  $p_{ij} = p_i -$   
166 p<sub>j</sub>. These definitions are given for each of the sensors in Figure S5b. Only five of the six  
167 available sensors were used.

168 The probe attachment component was manufactured by selective laser sintering 3D printing  
169 of nylon in two halves, as shown in Fig. S6A. The halves were bonded together using epoxy

170 with a layer of Tyvek between (Fig. S6A, right) to close off the channels and to provide  
171 channel routing between the layers through holes in the relevant areas. Tyvek was used  
172 because it is light weight and stretch resistant. Pressure probes were made from carbon fibre  
173 tube with 1.5 mm outer diameter and 0.7 mm internal diameter. The probe assembly ready for  
174 connection is illustrated in Fig. S6B.

175 We used a Propeller Mini microcontroller (Parallax Inc.) for receiving and processing the  
176 pressure sensor values (Fig. S7). It was modified from its original form by removing the  
177 portion of a board with a set of higher voltage regulators. This reduced the board size by  
178 more than half, as well as significantly reducing its mass. The microcontroller features a  
179 parallel architecture with eight separate cores that allow for parallel processing at a clock  
180 speed of 80 MHz. It was programmed to read pressure values (via I<sup>2</sup>C) from each of the six  
181 sensors at a rate of 1 kHz, and perform moving average and RMS computations on the  
182 readings. Algorithms monitored whether each channels surpassed pre-set thresholds  
183 corresponding to a floor or wall proximity condition.

184 To fit the sensor module to the quadcopter and allow it to receive on-board power, a second  
185 PCB was designed to adapt the connections to that of the Crazyflie (Fig. S7). This adapter  
186 board connects the microcontroller to the quadcopter I<sup>2</sup>C input bus, and was also fitted with

187 forward, back, and side-facing LEDs to provide a visual indication of the proximity condition  
188 as determined from the processed pressure sensor values. These individual components were  
189 designed to be modular, simply stacking on top of each other when fitted to the Crazyflie 2.0  
190 underside (Fig. S8).  
191

192 System architecture

193

194 The system architecture comprising the quadcopter, a pressure sensor array, connecting  
195 elements, guidance, navigation and control is shown in Figure S9. This consists primarily of  
196 the Crazyflie quadcopter platform, which is tracked in 3D space by an array of motion  
197 capture cameras that feed this positional data via UDP communication to a PC-based flight  
198 outer loop controller. The controller receives telemetry and commands the quadcopter to  
199 update its position via radio link.

200 The array of pressure sensors fitted around the quadcopter communicate via I<sup>2</sup>C to a  
201 dedicated microcontroller, which serves the sole function of receiving and filtering the  
202 pressure values. It then processes the pressure data streams to determine if a floor or wall is  
203 within close proximity, and – if so – in which direction it lies. The determination is based on  
204 pre-programmed pressure thresholds determined during tethered trials. A more sophisticated  
205 algorithm would characterise change in the pressure distribution as a function of throttle. If  
206 scaled to alternative platforms, the thresholds required are likely to be different from those  
207 we use here. However, since the mechanism is based on downwash and recirculation, there is  
208 no physical impediment for this type of surface detection working at all scales of rotorcraft

209 and flappercraft, so long as suitable thresholds are selected.

210 The microcontroller sends a ‘proximity condition’ to the quadcopter’s microcontroller. Here,

211 the proximity condition simply takes the form of an integer which has the representations

212 listed in Table S1. The quadcopter then displays the proximity condition by illuminating, or

213 otherwise, the four onboard display LEDs. It can also relay this proximity condition along

214 with its standard telemetry parameters (attitude, battery level, etc.) to the PC-based flight

215 controller.

216

217 Size, weight and power

218

219 The mass breakdown for the pressure sensor module along with the power consumption  
220 values are summarised in Table S2. The original quadcopter battery (240 mAh LiPo), was  
221 replaced with a battery of 38% lower mass (with 150 mAh capacity) as this improved the  
222 flight time when carrying the added payload of the pressure sensor module. With the  
223 exception of the protruding proximity condition indicator LEDs and pressure probes, the  
224 pressure sensor module measures  $39 \times 27 \times 14$  mm.

225

226 Pressure differential delta thresholds

227

228 From preliminary tethered flight tests, pressure thresholds were selected that correspond to a  
229 known floor or wall proximity conditions. A threshold of 0.5 Pa was chosen for a floor  
230 proximity condition, and 0.3Pa was selected for a wall forward / aft condition. The different  
231 combinations of bottom versus top pressure differential ( $P_{\Delta_{BT}}$ ) and forward versus aft  
232 differential ( $P_{\Delta_{FA}}$ ) values that correspond to the proximity conditions are summarised in  
233 Table S3. If the  $P_{\Delta_{BT}}$  and  $P_{\Delta_{FA}}$  values meet both conditions for a given row, then the

234 pressure sensor module has identified that the corresponding proximity condition has  
235 occurred. Algorithms were programmed into the pressure sensor module to identify proximity  
236 conditions from the listed pressure differential combinations. Starboard and port wall  
237 conditions have been excluded because wall detection in this direction is much less sensitive  
238 due to counter rotation of adjacent rotors. Fortunately, however, quadcopters can fly in any  
239 orientation so this is of little practical consequence.

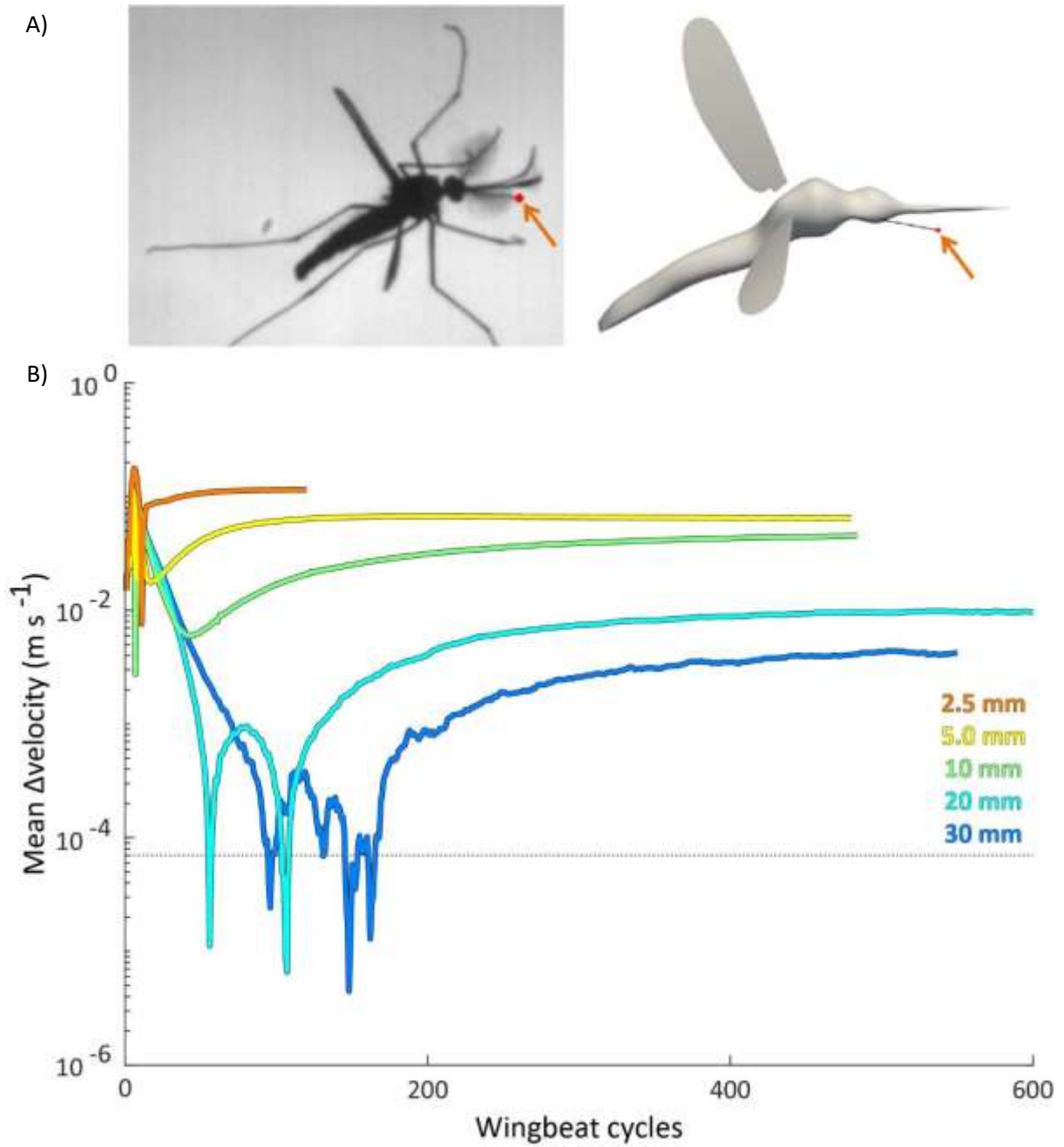
240

241 Autonomous flight arena

242

243 A schematic of the autonomous flight arena for providing closed-loop control of the  
244 quadcopter trajectory is shown in Fig. S10. As is becoming commonplace, the quadcopter  
245 was fitted with retroreflective markers tracked by 12 motion capture cameras (Qualisys; 100  
246 Hz) which provide marker coordinates in the calibrated lab space to a central computer. The  
247 computer runs an outer loop flight controller with the Linux Robot Operating System (ROS)  
248 that accepts the marker positions, computes the quadcopter position and orientation, and then  
249 transmits commands to the quadcopter to update its according to the set point error calculated  
250 in its current position and orientation.

251

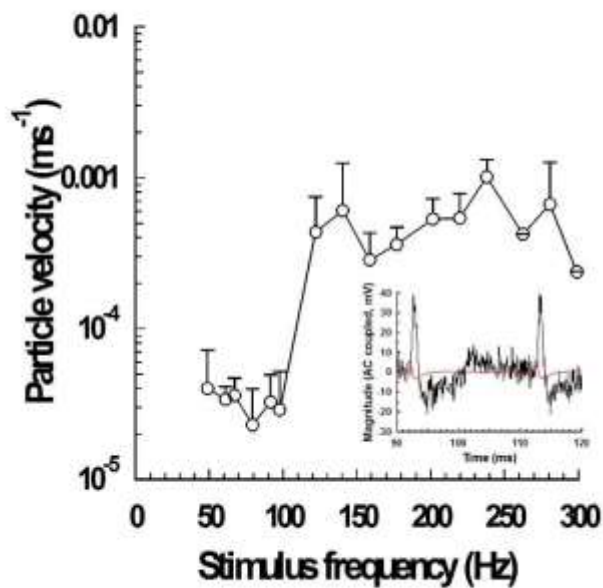


252

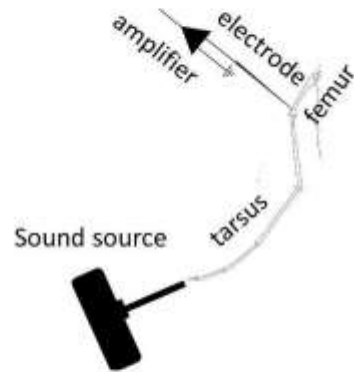
253 **Figure S1:** A) location of the antennal tip monitoring location relative to the mosquito body

254 reconstructed from multiple raw data images. B) convergence of the flow field velocity delta

255 with a varying number of wingbeat cycles at selected altitudes.



A)



B)

256

257 **Figure S2.** Particle velocity threshold (mean + S.D) as a function of stimulus frequency (A)

258 of neural responses recorded from the femurs of the hind legs in response to a vibrating air jet

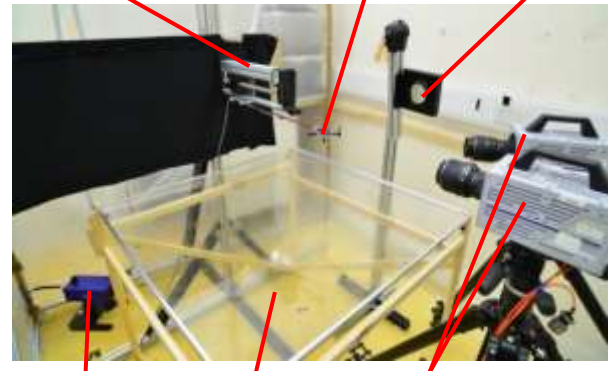
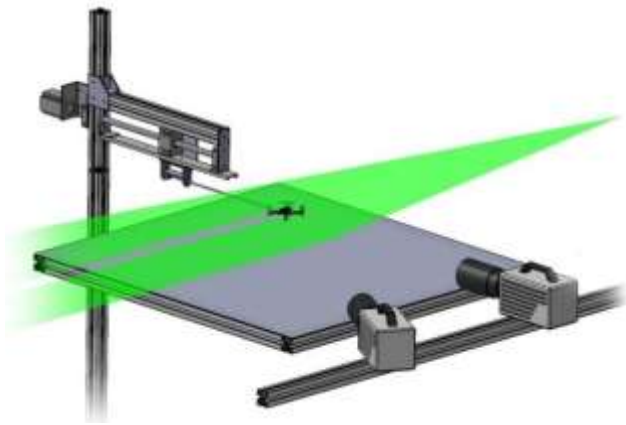
259 located 2 mm from the claws of the pretarsus with the jet directed parallel to the long axis of

260 the tarsus (B). Inset: Response of a mechanosensory neuron from a male mosquito femur.

261 Intracellular response (black) to the sound stimulus (50 Hz sinusoids, peak particle velocity

262  $5.4 \times 10^{-5} \text{ ms}^{-1}$ ) and output of particle velocity microphone (red) placed at the stimulus site

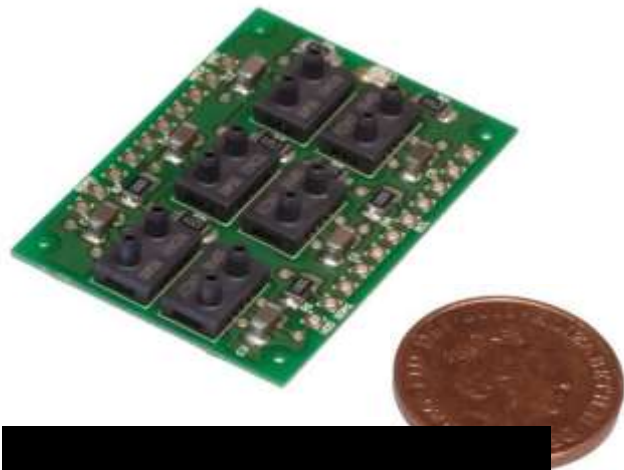
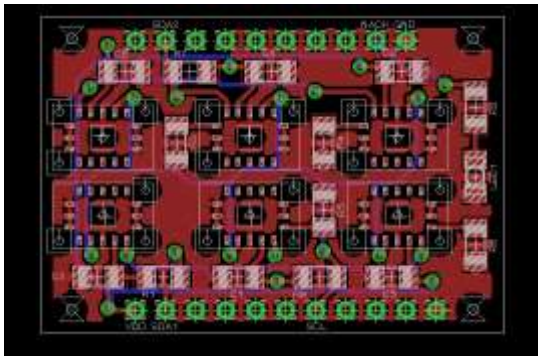
263 (pretarsus).



264

265 **Figure S3.** Flow field measurement setup; A) CAD model of apparatus; B) photograph taken

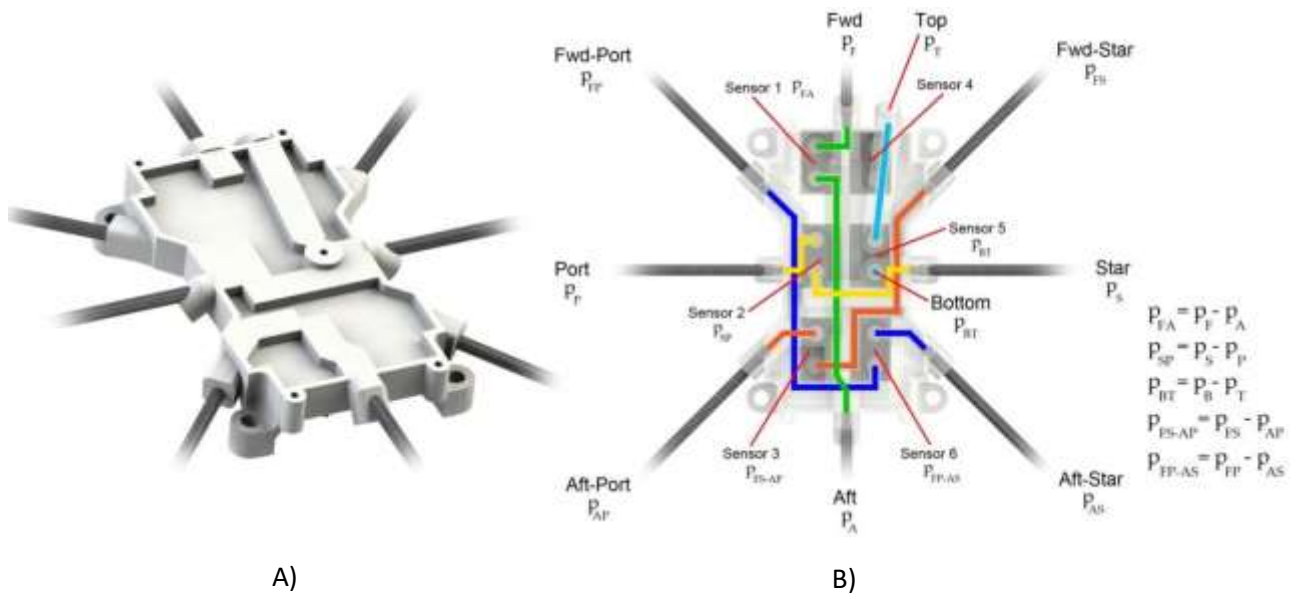
266 in the laboratory.



267

268 **Figure S4.** A) pressure sensor array PCB design; B) manufactured PCB fitted with six

269 differential pressure sensors.



270

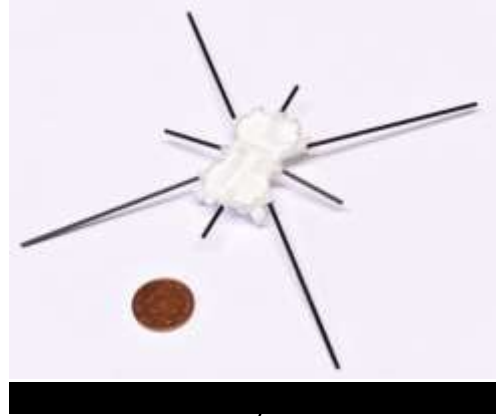
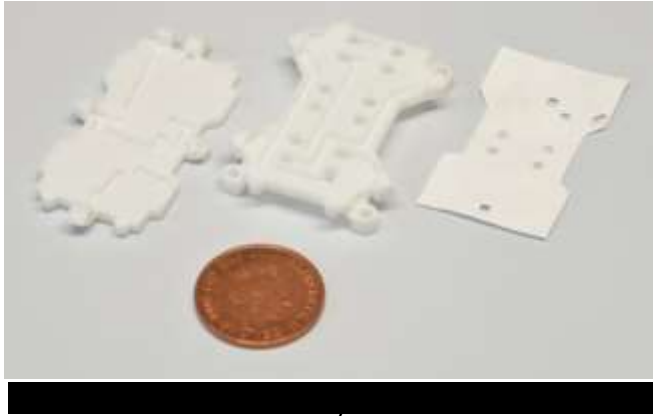
271

272

273 **Figure S5.** Pressure probe attachment; A) CAD model of attachment with extending pressure

274 ports; B) top view of mapping of pressure ports to differential pressure sensors and internal

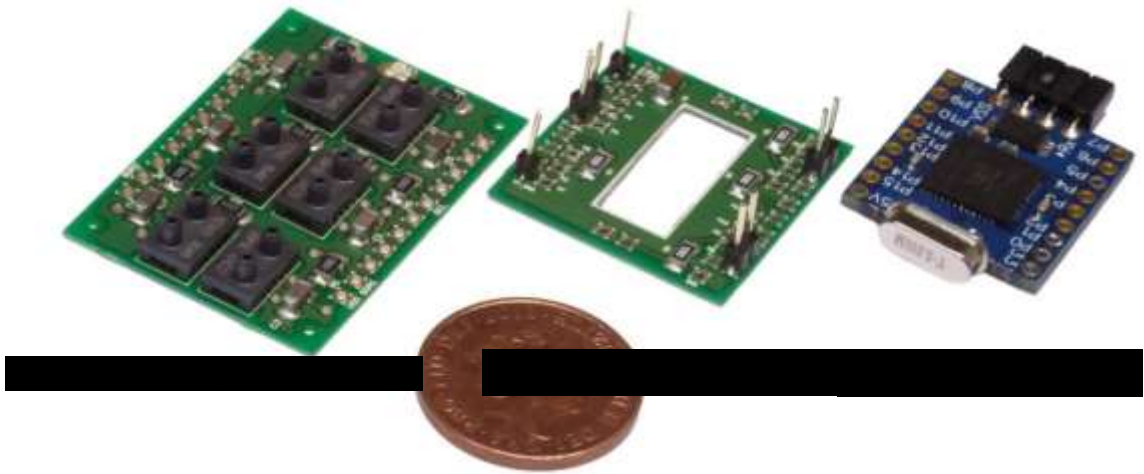
275 routing tracks (shown in colour) from sensors to ports; Sensor 4 is unused.



276

277 **Figure S6.** A) pressure probe attachment components; B) assembled pressure probe

278 attachment.



279

280 **Figure S7.** Pressure sensor module components; A) pressure sensor array; B) adapter PCB;

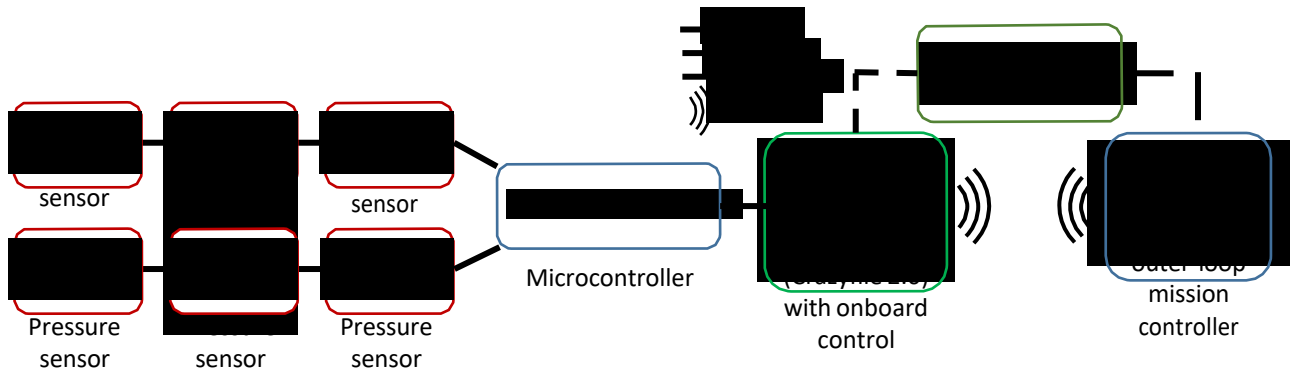
281 C) microcontroller.



282

283 **Figure S8.** Pressure sensor module fitted to the quadcopter underside.

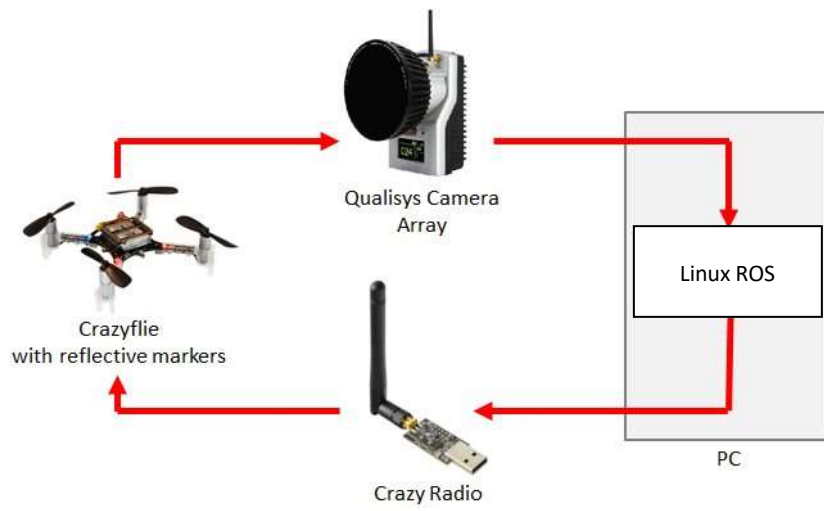
284



285

286 **Figure S9.** System block diagram of overall platform system architecture, and connection

287 types between elements.



288

289

290 **Figure S10:** Autonomous flight arena system block diagram.

291

<b>Proximity condition</b>	<b>Meaning</b>
0	No obstacles
1	Near floor proximity
2	Near wall proximity – forward direction
3	Near wall proximity – starboard direction
4	Near wall proximity – aft direction
5	Near wall proximity – port direction

292

293 **Table S1.** Proximity condition definitions.

<b>Component</b>	<b>Mass (g)</b>	<b>Current draw (mA)</b>	<b>Power (mW)</b>
microcontroller	2.5	4	12
pressure sensor array	2.4	19	57
adapter board	1.1	n/a	n/a
pressure probes	3.2	n/a	n/a
<b>Total:</b>	<b>9.2</b>	<b>23</b>	<b>69</b>

294

295 **Table S2.** Mass, current and power breakdown of pressure sensor module components.

<b>Proximity condition</b>	<b>Meaning</b>	<b><math>P\Delta_{BT}</math> condition</b>	<b><math>P\Delta_{FA}</math> condition</b>
0	No obstacles	$P\Delta_{BT} < 0.5$	$-0.3 < P\Delta_{FA} < 0.3$
1	Near floor proximity	$P\Delta_{BT} > 0.5$	$-0.3 < P\Delta_{FA} < 0.3$
2	Near wall proximity – forward direction	$P\Delta_{BT} < 0.5$	$P\Delta_{FA} < -0.3$
3	Near wall proximity – starboard direction	n/a	n/a
4	Near wall proximity – aft direction	$P\Delta_{BT} < 0.5$	$P\Delta_{FA} > 0.3$
5	Near wall proximity – port direction	n/a	n/a